Warm Molecular Gas in M51: Mapping the Excitation Temperature and Mass of H_2 with the Spitzer Infrared Spectrograph

Gregory Brunner[1,2]

Department of Physics and Astronomy, Rice University,

Houston, TX 77005

gbrunner@rice.edu

Kartik Sheth[3], Lee Armus[3]

Spitzer Science Center, Caltech, Pasadena, CA 91125

Mark Wolfire[4], Stuart Vogel[4]

Department of Astronomy, University of Maryland, College Park, MD 20741

Eva Schinnerer[5]

Max-Planck-Intitüt für Astronomie, Heidelberg, Germany

George Helou[3]

Spitzer Science Center, Caltech, Pasadena, CA 91125

Reginald Dufour[1]

Department of Physics and Astronomy, Rice University, Houston, TX 77005

John-David Smith[6]

University of Arizona, Steward Observatory, Tucson, AZ 85721

and

Daniel A. Dale[7]

Department of Physics and Astronomy, University of Wyoming, Laramie, WY 82071

– 2 –

Received ⎯⎯⎯⎯⎯⎯⎯⎯⎯⎯ ; accepted ⎯⎯⎯⎯⎯⎯⎯⎯⎯⎯

[1]Department of Physics and Astronomy, Rice University, Houston, TX 77005

[2]Visiting Graduate Student Fellow, Spitzer Science Center, Caltech, Pasadena, CA 91125

[3]Spitzer Science Center, Caltech, Pasadena, CA 91125

[4]Department of Astronomy, University of Maryland, College Park, MD 20741

[5]Max-Planck-Institüt für Astronomie, Heidelberg, Germany

[6]University of Arizona, Steward Observatory, Tucson, AZ 85721

[7]Department of Physics and Astronomy, University of Wyoming, Laramie, WY 82071

ABSTRACT

We have mapped the warm molecular gas traced by the H_2 $S(0) - H_2$ $S(5)$ pure rotational mid-infrared emission lines over a radial strip across the nucleus and disk of M51 (NGC 5194) using the Infrared Spectrograph (IRS) on the *Spitzer Space Telescope*. The six H_2 lines have markedly different emission distributions. We obtained the H_2 temperature and surface density distributions by assuming a two temperature model: a warm (T $= 100 - 300$ K) phase traced by the low J (S(0) – S(2)) lines and a hot phase (T $= 400 - 1000$ K) traced by the high J (S(2) – S(5)) lines. The lowest molecular gas temperatures are found within the spiral arms (T ~ 155 K), while the highest temperatures are found in the inter-arm regions (T > 800 K). The warm gas surface density reaches a maximum of 11.0 $M_\odot$ pc^{-2} in the north-western spiral arm, whereas the hot gas surface density peaks at 0.24 $M_\odot$ pc^{-2} at the nucleus. The spatial offset between the peaks in the warm and hot phases suggests that the warm phase is more efficiently heated by star formation activity and the hot phase is more efficiently heated by nuclear activity. The warm H_2 is found in the dust lanes of M51, spatially offset from the brightest Hα regions. The warm H_2 is generally spatially coincident with the colder (T ~ 10 K) molecular gas traced by CO (J $= 1 - 0$) emission, consistent with excitation of the warm phase in dense photodissociation regions (PDRs). In contrast, the hot H_2 is most prominent in the nuclear region; here the hot H_2 coincides with with [O IV](25.89 μm) and X-ray emission, indicating that shocks and/or X-rays are responsible for exciting this phase.

Subject headings: galaxies: ISM — galaxies: H_2 — galaxies: individual(M51)

1. Introduction

Star formation and galactic evolution are connected via the molecular gas in a galaxy. In the Milky Way, star formation occurs in molecular clouds, although not all clouds are actively forming stars. On a global, galactic scale, star formation may be triggered whenever the molecular gas surface density is enhanced, for example, by a spiral density wave (Vogel et al. 1988), by increased pressure or gas density in galactic nuclei (Young and Scoville 1991; Sheth et al. 2005), by hydrodynamic shocks along the leading edge of bars (Sheth et al. 2000; Sheth et al. 2002), and in the transition region at the ends of bars (Kenny and Lord 1991; Sheth et al. 2002). How does this star formation affect the surrounding molecular gas? How is it heated and what is the distribution of the gas temperatures? How does the mass of the warm and hot gas vary from region to region? We address these questions using spectral line maps from a radial strip across the grand-design spiral galaxy, M51.

M51 (the Whirlpool galaxy, NGC 5194) is a nearby, face-on spiral galaxy that is rich in molecular gas. Its proximity (assumed to be 8.2 Mpc (Tully 1988)), face-on orientation, and grand-design spiral morphology make it the ideal target for studies of the interstellar medium (ISM) across distinct dynamical, chemical, and physical environments in a galaxy. Studies of the molecular gas within M51 have revealed giant molecular associations (GMAs) along the spiral arms (Vogel et al. 1988; Rand and Kulkarni 1990; Aalto et al. 1999), a reservoir of molecular gas in the nuclear region that is massive enough to fuel the active galactic nucleus (AGN) (Scoville et al. 1998), and spiral density wave triggered star-formation in molecular clouds (Vogel et al. 1988). In addition to being well-studied at millimeter and radio wavelengths, M51 has also been studied at X-ray, UV, optical, near-infrared, infrared, and submillimeter wavelengths (Palumbo et al. 1985; Terashima et al. 1998; Scoville et al. 2001; Calzetti et al. 2005; Matsushita et al. 2004).

In this paper we present maps of the H_2 S(0) − H_2 S(5) pure rotational mid-infrared lines over a strip across M51 created from *Spitzer Space Telescope* Infrared Spectrograph (IRS) spectral mapping mode observations. The mid-infrared H_2 lines trace the warm (T = 100 – 1000 K) phase of H_2 and we use these lines to model the H_2 excitation-temperature, mass (Rigopoulou et al. 2002; Higdon et al. 2006), and ortho-to-para ratio (Neufeld et al. 1998; Neufeld et al. 2006) across the M51 strips.[1] We use the inferred distributions to place constraints on the energy injection mechanisms (i.e. radiative heating, shocks, turbulence) that heat the warm molecular gas phase of the ISM.

2. Observations and Data Reduction

2.1. Spectral Data

We mapped a radial strip across M51 using the short-low (SL; 5 – 14.5 μm) and long-low (LL; 14 - 38 μm) modules of the *Spitzer* IRS in spectral mapping mode (Houck et al. 2004). The radial strips were $324'' \times 57''$ and $295'' \times 51''$ in the SL and LL, respectively. Each slit position was mapped twice with half-slit spacings. In total, 1,412 spectra were taken in the SL and 100 were taken in the LL. Integration times for individual spectra were 14.6 s in both the SL and LL. Dedicated off-source background observations were taken for the SL observations. Backgrounds for the LL observations were taken from outrigger data collected while the spacecraft was mapping in the adjacent module. Uncertainties in IRS fluxes are on the order of 25% (Smith et al. 2004). The astronomical observation requests (AORs) are available on SST's Leopard and Spot (Project ID 200138, PI: K. Sheth).

---

[1]While we are always exploring the warm phase of H_2, in this paper we refer to a warm and a hot phase corresponding to temperatures of T = 100 – 300 K and T = 400 – 1000 K, respectively.

The spectra were assembled from the basic calibration data (BCD) into spectral data cubes for each module using CUBISM (Kennicutt et al. 2003; Smith et al. 2004; Smith et al. 2007a). Background subtraction and bad pixel removal were done within CUBISM. The individual BCDs were processed using the S14.0 version of the Spitzer Science Center (SSC) pipeline. In CUBISM, the SL and LL data cubes have $1\farcs85$ and $5\farcs08$ pixels, respectively. This pixel size is half the full width at half maximum (FWHM) of the point spread function (PSF) at the red end of a given module. In principle, the PSF should vary with wavelength but since the PSF is undersampled at the blue end of the module, it is approximately constant across a given module. So the approximate resolution of the SL and LL modules is $3\farcs7$ and $10\farcs1$, respectively.

We created continuum-subtracted line intensity maps of the H_2 S(0) $-$ H_2 S(5) lines using a combination of PAHFIT (Smith et al. 2007b) and our own code. PAHFIT is a spectral fitting routine that decomposes IRS low resolution spectra into broad PAH features, unresolved line emission, and grain continuum with the main advantage being that it allows one to recover the full line flux of any blended features. It also solves for the foreground dust emission and dereddens the emitted line intensities. Several H_2 lines are blended: H_2 S(1) with the 17.0 μm PAH complex, H_2 S(2) with the 12.0 and 12.6 μm PAH complexes, and the H_2 S(5) with the [Ar II](6.9 μm) line. We first concatenated SL1 and SL2, and LL1 and LL2 data cubes into two cubes, one for SL and one for LL. We smoothed each map in the cubes by a 3×3 pixel box, conserving the flux, to increase the signal-to-noise ratio of the spectra. Then, for each pixel, we extracted a spectrum and ran PAHFIT to decompose it. We saved the location of the pixel on the sky along with the PAHFIT output (i.e. integrated line flux, line FWHM, line equivalent width, the uncertainty in the line flux, the fit to the entire spectrum and the fit to the continuum) for each spectrum and used this information to construct line flux maps for all of the mid-infrared features. In addition to creating line maps, we created maps of line FWHM, line equivalent width, and uncertainty

in the flux and data cubes of the fit to the entire spectrum, the fit to the continuum, a continuum-subtracted data cube, and a residual data cube. In this paper we focus primarily on the H_2 line maps.

2.2. Ancillary Data: CO (J = 1 − 0), Hα, and X-ray Observations

In this section we briefly discuss the ancillary data that we have used in order to understand H_2 excitation in M51. We take note of the image resolutions for comparison to *Spitzer* IRS beam. The Berkely Illinois Maryland Array (BIMA) CO (J = 1 − 0) map was acquired as part of the BIMA Survey of Nearby Galaxies (SONG) (Regan et al. 2001; Helfer et al. 2003). At the distance of M51, the SONG beam ($5''8 \times 5''1$) subtends 220 pc × 190 pc. The continuum-subtracted Hα + [N II] image of M51 was obtained from the *Spitzer Infrared Nearby Galaxies Survey* (SINGS) archive.[2] The native pixel scale for the image is $0''3$ and the angular resolution is $\sim 1''$. X-ray emission from M51 was observed by the Advanced CCD Imaging Spectrometer (ACIS) on the *Chandra X-Ray Observatory* on 20 June 2000. The resolution of the image is $\sim 1''$. The X-ray image that we use has been presented and discussed in Terashima and Wilson (2001).

3. Results

3.1. The Distribution of H_2 Emission

We have detected and mapped H_2 emission from the six lowest pure rotational H_2 lines (Figure 1). The maps reveal remarkable differences in the distribution of H_2 emission in M51. H_2 S(0) emission is strongest in the northwest inner spiral arm peaking at a flux of

---

[2]http://data.spitzer.caltech.edu/popular/sings/

3.7×10^{-18} W m^{-2} and decreases by a factor of 2 in the nuclear region. In contrast, the H$_2$ S(1) emission peaks in the nucleus of the galaxy at 1.0×10^{-17} W m^{-2} and has an extension of equal brightness towards the northwest inner spiral arm. In the spiral arm itself, the H$_2$ S(0) peak is offset from the H$_2$ S(1) emission by 10$''$ ($\sim$ 380 pc). We detect emission from the H$_2$ S(0) and H$_2$ S(1) lines to the outer limit of our radial strip, $\sim$ 6 kpc from the nucleus of the galaxy. In the outer spiral arms, the H$_2$ S(0) flux is a factor of 2 times lower than in the inner northwest spiral arm and the H$_2$ S(1) flux is a factor of 5 times lower than in the nucleus.

The H$_2$ S(2) $-$ H$_2$ S(5) maps show different molecular gas distributions within M51 through each H$_2$ line. The brightest H$_2$ S(2) emission is from the nucleus at 2.2×10^{-18} W m^{-2}. We also see bright H$_2$ S(2) emission from the inner northwest spiral arm at half the flux of the nuclear peak. The H$_2$ S(3) peak at the nucleus is 1.4×10^{-17} W m^{-2}, a factor of $\sim$ 6 greater than the H$_2$ S(2) nuclear peak. There is also a linear bar-like structure in H$_2$ S(3) emission across the nucleus of the galaxy at a PA$\sim$-10^0. The emission peaks in the H$_2$ S(2) and H$_2$ S(3) maps are not spatially coincident. For instance, in the northwest inner spiral arm the brightest H$_2$ S(3) emission is further down the spiral arm than the brightest H$_2$ S(2) emission. Offsets like these suggest variations in the excitation temperature from region to region within a galaxy, and even within a spiral arm.

The H$_2$ S(4) and H$_2$ S(5) lines are brightest at the nucleus with fluxes of 3.1 and 8.0 $\times$ 10^{-18} W m^{-2}, respectively. The H$_2$ S(4) line shows emission in the nucleus and in the spiral arm to the west. In the spiral arm to the west of the nucleus, the H$_2$ S(4) flux is 2.1 $\times$ 10^{-18} W m^{-2}. This is notable because the spiral arm to the southwest of the nucleus is very bright in CO and and studies have revealed very high molecular gas column densities in the southwest inner spiral arm (Lord and Young 1990; Aalto et al. 1999). H$_2$ S(5) emission is asymmetric in the nucleus and mimics the morphology of the H$_2$ S(3) line with extended

emission to the north of the nucleus.

3.2. Mapping H$_2$ Excitation Temperature and Surface Density across M51

3.2.1. Modeling H$_2$ Excitation Temperature and Surface Density

The pure rotational lines of molecular hydrogen provide a powerful probe of the conditions of the ISM by placing constraints on the energy injection that excites H$_2$. For example, Neufeld et al. (2006) discuss shock excitation of H$_2$ and Kaufman et al. (2006) discuss H$_2$ excitation in photodissociation regions (PDRs). Using the maps of H$_2$ emission, we modeled the H$_2$ temperature and mass distribution over the radial strip in M51 following the methods described in Rigopoulou et al. (2002) and Higdon et al. (2006).

First, we smoothed the H$_2$ S(1) − H$_2$ S(5) maps to the resolution of the H$_2$ S(0) map, $10\rlap{.}{''}1$. The maps were then interpolated to the same spatial grid. Excitation diagrams across the strip were derived from the Boltzmann equation

$$N_i/N = (g(i)/Z(\mathrm{T_{ex}}))exp(-T_i/\mathrm{T_{ex}}) \tag{1}$$

where $g(i)$ is the statistical weight of state i, $\mathrm{Z(T_{ex})}$ is the partition function, $\mathrm{T_i}$ is the energy level of a given state, and $\mathrm{T_{ex}}$ is the excitation temperature. N and $\mathrm{N_i}$ are the total column density and the column density of a given state i and $\mathrm{N_i}$ is determined directly from the measured extinction-corrected flux by

$$N_i = 4\pi \times flux(i)/(\Omega A(i)h\nu(i)) \tag{2}$$

where A(i) is the Einstein A-coefficient, $\nu(i)$ is the frequency of state i, Ω is the solid angle of the beam, and h is Planck's constant. Table 1 lists the values for the wavelength, rotational state, Einstein A-coefficient, energy, and statistical weight of the pure rotational levels of H$_2$.

In order to derive temperature and surface density distributions we assume a two temperature model for the H_2. To determine the hot (T = 400 – 1000 K) phase temperature, we do a least squares fit to the H_2 S(2) – H_2 S(5) column densities in the excitation diagram at every pixel in our maps. We then subtract the contribution of the hot phase from the lower J lines and do a least squares fit to the column densities of H_2 S(0) – H_2 S(2) lines at every pixel in our maps to determine the temperature distribution of the warm (T = 100 – 300 K) phase. The warm and hot phase surface density distributions are derived from the column densities of the H_2 S(0) and H_2 S(3) lines, respectively. The column densities are easily converted to mass surface density by determining the mass of the warm and hot H_2 within every pixel.

Figure 2 shows excitation diagrams and the fits to the warm and hot H_2 phases for three different regions across the M51 strip. The three regions are marked on the H_2 surface density maps in Figure 3. In the nuclear region (Region 2) the ortho and para levels appear to lie along the same curve indicating an ortho-to-para ratio (OPR) of 3; the excitation diagrams do not exhibit the "zigzag" characteristic of a non-equlibrium H_2 OPR (Neufeld et al. 1998; Fuente et al. 1999). The slope of the curve appears to decrease as the rotational state increases indicating that we are sampling a continuous range of H_2 temperatures with the higher rotational states (S(2) – S(5)) probing a hotter phase of H_2 than the lower rotational states (S(0) – S(2)). In the southeast and northwest spiral arms (Regions 1 and 3, respectively) the lower J (H_2 S(0) - H_2 S(3)) levels exhibit an OPR of $\sim$ 3. The H_2 S(4) measurement shows significant scatter in the excitation diagrams outside of the nuclear region of M51. This would indicate that the OPR is less than 3, however, due to the low signal-to-noise ratio of the H_2 S(4) map, we do not believe that the OPR determined from the H_2 S(4) flux reflects the OPR of the warm H_2. We assume an OPR of 3 when deriving the H_2 temperature and mass distributions.

3.2.2. Warm and Hot H_2 Excitation Temperature and Surface Density Distributions

Figure 3 presents the warm (*left*) and hot (*right*) H_2 surface density distributions across the M51 strip.[3] The highest gas surface density for the warm H_2 phase is in the inner northwest spiral arm at 11 $M_\odot$ pc^{-2}. The gas surface density in the outer northwest and southeast spiral arms is maximum at the center of the spiral arms at 3.5 $M_\odot$ pc^{-2} and 1.0 $M_\odot$ pc^{-2} respectively. The hot phase surface density is highest in the nucleus and interior to the inner spiral arm at 0.24 $M_\odot$ pc^{-2}. The gas surface density of the hot phase in the spiral arms is 3 – 5 times lower than that of the nuclear region.

Figures 4 and 5 show the distribution of the warm and hot H_2 temperatures (in grayscale) with the contours of the warm and hot H_2 surface densities overlaid, respectively. In both cases we see that the temperature and surface density are inversely correlated with the hottest temperatures corresponding to regions of lowest surface density. For both the warm and hot phases, we see the temperature is higher in the inter-arm regions than in the spiral arms. We believe that this is real and does not result from lower signal-to-noise in the inter-arm regions. A lower signal-to-noise ratio would increase the slope of the line in the least squares fit to the warm and hot H_2 excitation diagrams and result in a lower temperature.

Figure 6 compares the warm (in grayscale) and hot (in contours) H_2 surface density distributions. The warm H_2 mass distribution peaks in the northwest inner spiral arm and the hot H_2 mass distribution peaks in the nucleus and in the region interior to the northwest spiral arm. The warm-to-hot H_2 mass ratio is not constant across the galaxy but is lowest (~ 12) in the nucleus of the galaxy and increases to 170 and 136 in the southeast

---

[3]Note that the non-rectangular shape of the strip is due to the offset between the SL and LL strips.

and northwest spiral arms, respectively.

4. Discussion

4.1. Warm and Hot H_2 in M51

Previous studies have used aperture-averages over entire galactic nuclei to derive the physical conditions of the molecular gas (Rigopoulou et al. 2002; Higdon et al. 2006; Roussel et al. 2007). In M51, Roussel et al. (2007) find that within the central 330 arcsec^2 (4.61×10^5 pc^2), the warm H_2 phase has a temperature of 180 K and a surface density of 3.2 $M_\odot$ pc^{-2} (a total mass of $M_{warm} = 1.5 \times 10^6$ $M_\odot$). Roussel et al. (2007) have also measured the temperature of the hot phase (though they do not measure the mass in the hot phase) and find a hot H_2 temperature of 521 K.

Having spatially resolved spectra over a strip across M51, we can investigate the behavior of the warm and hot H_2 phases on smaller scales. In the nuclear region of M51 we see that the warm phase temperature peaks at 192 K and decreases radially towards the inner spiral arms. The warm H_2 surface density at the nucleus is 4.4 $M_\odot$ pc^{-2} and decreases over a 0.5 kpc radius surrounding the nucleus. To check the consistency of our results against those of Roussel et al. (2007), we averaged the warm phase temperature over a similar 412 arcsec^2 (5.76×10^2 pc^2) aperture and found that the warm phase temperature and surface density are 186 K and 2.8 $M_\odot$ pc^{-2}, respectively. These results suggests that previous studies of the warm H_2 temperature and mass have yielded average values rather than a maximum values.

4.2.   Distinguishing the H_2 Excitation Mechanisms

The warm-to-hot H_2 surface density ratio varies across M51 suggesting that the H_2 excitation mechanisms have different effects on the warm and hot phases. The largest warm H_2 surface densities are found in the spiral arms suggesting that the warm phase is associated with star formation activity. The largest hot H_2 surface densities are found in the nuclear region of M51 suggesting that the hot phase is more efficiently excited by nuclear activity. Roussel et al. (2007) find that H_2 is generally heated by massive stars in PDRs, however, Seyferts and LINERs show evidence for the dominance of other excitation mechanisms such as X-rays or shocks. By comparing the spatial distribution of the warm and hot H_2 to $H\alpha$ and CO ($J = 1 - 0$) emission, we can investigate the relationship between star formation and H_2. Additionally, by comparing the warm and hot H_2 distributions to X-ray observations and the spatial distribution of [O IV]($25.89~\mu$m) emission, we can investigate X-ray and shock heating of H_2 within M51.

Kaufman et al. (2006) show that within galaxies, where the telescope beam size is generally kiloparsecs across, H_2 emission could serve to probe the average physical conditions in the surfaces of molecular clouds. In Figure 7, we compare the warm ($left$) and hot H_2 ($right$) mass distributions to the cold (T ~ 10 K) phase of H_2 traced by CO ($J = 1 - 0$) emission. The warm and hot H_2 phases appear to trace the bright CO emission in the northwest and southeast spiral arms. Comparison of CO to the individual H_2 S(0) $- H_2$ S(3) line intensity maps in Figure 8 also shows that the H_2 in the spiral arms traces the bright CO emission. In the spiral arms, both the warm and hot H_2 phases are found in PDRs and are associated with star formation activity. The most striking result is that in the inner spiral arms, we see that the CO is offset toward the nucleus from the warm H_2 mass (in Figure 7). The offset between the peaks in CO and warm H_2 mass is $7''$ in the northwest inner spiral arm and $5''$ in the southeast inner spiral arm. We believe that these

offsets are real with one possible explanation being that the H_2 is tracing the regions of active star-formation within the giant molecular associations.

In Figure 9, we compare the warm ($left$) and hot ($right$) H_2 mass distributions to $H\alpha$ emission. In general, the warm and hot H_2 concentrations are not cospatial with the brightest $H\alpha$ emission regions in the spiral arms with the one exception being that the warm H_2 mass in the northwest and southeast inner spiral arms appears to trace the $H\alpha$ emission. The warm H_2 mass contours show that local peaks in H_2 mass are found within the dust lanes. An example of this is in the northwest spiral arms where we see the H_2 mass offset from the $H\alpha$ spiral arms with local peaks being found in the dust lanes. In Figure 10, we compare the H_2 S(0) $-$ H_2 S(3) line intensity maps to $H\alpha$ emission. Comparison of the H_2 S(0) map to $H\alpha$ reveals that the strongest H_2 emission in the northwest and southeast inner spiral arms is coincident with $H\alpha$ emission; however, the other H_2 S(0) spiral arms show the strongest emission in the dust lanes, offset from the $H\alpha$ spiral arms. The largest offsets are seen in the southeast spiral arm where the H_2 S(0) emission is offset from the $H\alpha$ spiral arm by $\sim 15''$ (560 pc). H_2 S(1) emission appears to follow the dust lanes and the H_2 S(1) intensity subsides into the $H\alpha$ spiral arms. H_2 S(2) and H_2 S(3) emission is also found in the dust lanes; however, there are instances (such as in the southeast spiral arm) where the H_2 emission appear to be found straddling the dust lane and $H\alpha$ spiral arm.

The [O IV](25.89 μm) line can be excited in fast shocks ($v_s > 100$ km s^{-1}) (Lutz et al. 1998), by photoionization in Wolf-Rayet stars (Schaerer and Stasinska 1999), or by an AGN (Smith et al. 2004). Though the [O IV] line is blended with the [Fe II](25.99 μm) line in $Spitzer$ IRS low resolution spectra, PAHFIT can deblend the two lines and in mapping the H_2 S(0) and H_2 S(1) lines in the LL data cubes we also mapped the [O IV] line. In Figure 11, we compare the [O IV] surface brightness to the warm ($left$) and hot ($right$) H_2 disributions. The [O IV] emission is brightest in the nuclear region at 8.7 $\times$

10^{-18} W m^{-2} and the peak is coincident with the nuclear peak in the mass of the hot H$_2$. [O IV] surface brightness decreases from the nucleus to the inner spiral arm by 50 %. We resolve weaker [O IV] emission within the warm and hot H$_2$ spiral arms. The [O IV] surface brightness is a factor of ~ 6 lower in the spiral arms than the peak intensity found in the nucleus. The [O IV] emission within the nuclear region of M51 is likely due to the weak Seyfert II nucleus (Ford et al. 1985) and is possibly associated with shocked gas from the outflows of the AGN. The peak of the [O IV] emission coincides with the nuclear peak in hot H$_2$ mass, indicating that the hot H$_2$ phase in the nuclear region of the galaxy is AGN or shock heated. In the nuclear region we observe a factor of 12 times greater warm H$_2$ mass than the hot H$_2$ mass. The warm H$_2$ mass is much greater within the spiral arms than within the nucleus and the warm-to-hot mass ratio is lowest in the nuclear region where the [O IV] flux is greatest. The coincidence of [O IV] emission and the hot H$_2$ suggests that nuclear activity and shocks appear to be a more efficient means to excite the hot H$_2$ phase than the warm H$_2$ phase.

X-ray studies of M51 have revealed bright X-ray emission from the nucleus, the extranuclear cloud (XNC, to the south of the nucleus), and the northern loop (Terashima and Wilson 2001). A radio jet that is believed to be shock heating the ISM has been observed emanating from the south of the nucleus towards the XNC in 6 cm imagery (Crane and van der Hulst 1992). In Figure 12, we compare the smoothed 0.5 - 10 keV band X-ray image to the warm (*left*) and hot (*right*) H$_2$ mass distributions. The 0.5 - 10 keV band has been smoothed to the resolution of the warm and hot H$_2$ mass distributions and the nucleus, XNC, and northern loop are indistinguishable in the smoothed image. X-ray emission is brightest in the nucleus and decreases into the northwest spiral arm that contains the greatest H$_2$ mass. There appears to be very little connection between the 0.5 - 10 keV X-ray band and the warm H$_2$ mass distribution. The peak in X-ray emission is coincident with the hot H$_2$ mass peak. The brightest 0.5 - 10 keV X-ray emission originates

from the nucleus and is oriented north-to-south, similar to the [O IV](25.89 μm) emission. The peak in X-ray emission is located within the peak in hot H_2 mass suggesting that X-rays play an important role in exciting the hot H_2 phase. While there is a correlation between X-ray emission and the hot H_2 phase, H_2 excitation by X-rays cannot be distinguished from H_2 excitation by shocks. In Figure 13, we compare the X-ray surface brightness to the H_2 $S(2) - H_2$ $S(5)$ maps and find that the nuclear H_2 emission appears to be correlated with the X-ray source.

5. Conclusions

We have spectrally mapped a strip across M51 using the *Spitzer* IRS low resolution modules. We used the spatially resolved spectra to map H_2 $S(0) - H_2$ $S(5)$ lines across the strip. We find:

1. The distribution of H_2 emission in M51 varies with H_2 rotational level. H_2 $S(0)$ emission is brightest in the spiral arms of the galaxy while the higher J transitions show the strongest emission towards the nucleus. The H_2 $S(1)$ line is brightest in the nuclear region and is offset from the peak in H_2 $S(0)$ intensity in the inner northwest spiral arm by $10''$. The H_2 $S(2)$ and H_2 $S(3)$ maps show H_2 emission in the nucleus, spiral arms, and inter-arm regions of M51 and bar structure aligned north-to-south is apparent in H_2 $S(3)$ emission. H_2 $S(4)$ and H_2 $S(5)$ emission is resolved in the nuclear region of M51.

2. The different distributions of H_2 emission in M51 indicate significant spatial variations in H_2 temperature and surface density. Using the low J $(S(0) - S(2))$ lines to trace the warm (T $= 100 - 300$ K) H_2, we find that the warm H_2 temperature is highest in the nuclear region at 192 K and the warm H_2 surface density peaks in the northwest inner spiral arm at 11 $M_\odot$

pc^{-2}. Using the higher J (S(2) – S(5)) lines to trace the hot (T $= 400 - 1000$ K) H_2, we find that the hot H_2 temperature is lowest in the inner spiral arms ($500 - 550$ K) and increases to ~ 600 K in the nucleus where the largest hot H_2 surface density is found to be 0.24 $M_\odot$ pc^{-2}.

3. The warm and the hot H_2 surface density distributions are not cospatial and the warm-to-hot surface density ratio varies across M51. The warm H_2 surface density distribution peaks in the northwest spiral arm and is offset from the hot mass peak by $11''$. The hot H_2 surface density distribution shows two peaks, one in the nucleus of M51 and one located interior to the northwest inner spiral arm of M51. Variations in the warm-to-hot H_2 ratio and differences in the distributions of the H_2 line emission across M51 suggest that the warm H_2 is more efficiently heated by UV photons in star forming regions while the hot H_2 is more efficiently heated by shocks or X-rays associated with nuclear activity.

4. The warm H_2 traces the cold (T ~ 10 K) H_2 in the spiral arms of M51 indicating that the warm phase is associated with the surface layers of dense molecular clouds. The H_2 S(0) $-$ H_2 S(3) contours trace the CO; however, within the spiral arms, the peaks in H_2 can be offset from the peaks in CO intensity. In the nucleus, the H_2 S(1) – H_2 S(3) lines are brightest and the CO intensity is a factor of ~ 2.5 weaker than in the spiral arms suggesting that H_2 emission from the higher J lines is more efficiently excited by nuclear activity, shocks, or X-rays.

5. Comparing the distributions of H_2 to Hα reveals that the warm and hot H_2 in the spiral arms is found in the dust lanes rather than spatially coincident with the Hα emission regions.

6. [O IV](25.89 μm) emission and X-ray intensity peak in the nuclear region of M51 and their peaks are spatially coincident with the peak in hot H_2 surface density. This

implies that the hot H_2 is more efficiently heated by the AGN, shocks (possibly associated with the AGN), or X-rays associated with the AGN. The spatial distributions of the [O IV] emission and X-ray surface brightness are very similar preventing the characterization of the primary excitation mechanism (shocks or X-rays) of the hot H_2 phase in the nuclear region.

REFERENCES

Aalto, S., Huttemeister, S., Scoville, N.Z., and Thaddeus, P., 1999, AJ, 522, 165

Calzetti, D. et al., 2005, ApJ, 633, 871

Crane, P.C. and van der Hulst, J.M., 1992, AJ, 103, 1146

Ford, H.C., Crane, P.C., Jacoby, G.H., Lawrie, D.G., and van der Hulst, J.M., 1985, ApJ, 293, 132

Fuente, A., Martín-Pintado, J., Rodríguez-Fernández, N.J., Rodríguez-Franco, A., de Vicente, P., and Kunze, D., 1999, ApJ, 518, L45

Helfer, T.T., Thornley, M.D., Regan, M.W., Wong, T., Sheth, K., Vogel, S.N., Blitz, L., and Bock, D.C.J., 2003, ApJS, 145, 259

Higdon, S.J.U., Armus, L., Higdon, J.L., Soifer, B.T., and Spoon, H.W.W., 2006, ApJ, 648, 323

Houck, J.R. et al., 2004, ApJS, 145, 18

Kaufman, M.J., Wolfire, M.G., and Hollenbach, D.J., 2006, ApJ, 644, 283

Lord, S.D. and Young, J.S., 1990, ApJ, 356, 135

Lutz, D., Kunze, D., Spoon, H.W.W., and Thornley, M.D., 1998, A&A, 333, L75

Kennicutt, R.C. et al., 2003, PASP, 115, 928

Kenny, J.D.P. and Lord, S.D., 1991, ApJ, 381, 118

Matsushita, S. et al., 2004, ApJ, 616, L55

Neufeld, D.A., Melnick, G.J., and Harwit, M., 1998, ApJ, 506, L75

Neufeld, D.A., Melnich, G.J., Sonnentrucker, P., Bergin, E.A., Green, J.D., Kim, K.H., Watson, D.M., Forrest, W.J., and Pipher, J.L., 2006, ApJ, 649, 816

Palumbo, G.G.C., Fabbiano, G., Fransson, C., and Trinchieri, G., 1985, ApJ, 298, 259

Rand, R.J. and Kulkarni, S.R., 1990, ApJ, 349, L43

Regan, M.W., Thornley, M.D., Helfer, T.T., Sheth, K., Wong, T., Vogel, S.N., Blitz, L., and Bock, D.C.J., 2001, ApJ, 561, 218

Rigopoulou, D., Kunze, D., Lutz, D., Genzel, R., and Moorwood, A.F.M., 2002, A&A, 389, 374

Roussel, H. et al., 2007, in press

Schaerer, D. and Stasinska, G., 1999, A&A, 345, L17

Scoville, N.Z. and Young, J.S., 1983, AJ, 265, 148

Scoville, N.Z., Yun, M.S., Armus, L., and Ford, H., 1998, ApJ, 493, L63

Scoville, N.Z., Polletta, M., Ewald, S., Stolovy, S.R., Thompson, R., and Rieke, M., 2001, AJ, 122, 3017

Sheth, K., Regan, M.W., Vogel, S.N., and Teuben, P.J., 2000, ApJ, 532, 221

Sheth, K., Vogel, S.N., Regan, M.W., Tueben, P.J., Harris, A.I., and Thornley, M.D., 2002, AJ, 124, 2581

Sheth, K., Vogel, S.N., Regan, M.W., Thornley, M.D., and Teuben, P.J., 2005, ApJ, 632, 217

SINGS: The Spitzer Infrared Nearby Galaxies Fouth Data Delivery, May 2006.

Smith, J.D.T. et al., 2004, ApJS, 154, 199

Smith, J.D.T. et al., 2007, PASP, submitted

Smith, J.D.T. et al., 2007, ApJ, 656, 770

Terashima, Y., Ptak, A., Fujimoto, M.I., Kunieda, H., Makishima, K., and Sherlemitsos, P.J., 1998, ApJ, 496, 210

Terashima, Y. and Wilson, A.S., 2001, ApJ, 560, 139

Tully, R.B. 1988, Nearby Galaxies Catalog (Cambridge: Cambridge University Press)

Vogel, S.N., Kulkarni, S.R., and Scoville, S.Z., 1988, Nature, 334, 402

Young, J.S. and Devereux, N.A., 1991, ApJ, 373, 414

Young, J.S. and Scoville, N.Z., 1991, ARA&A, 29, 581
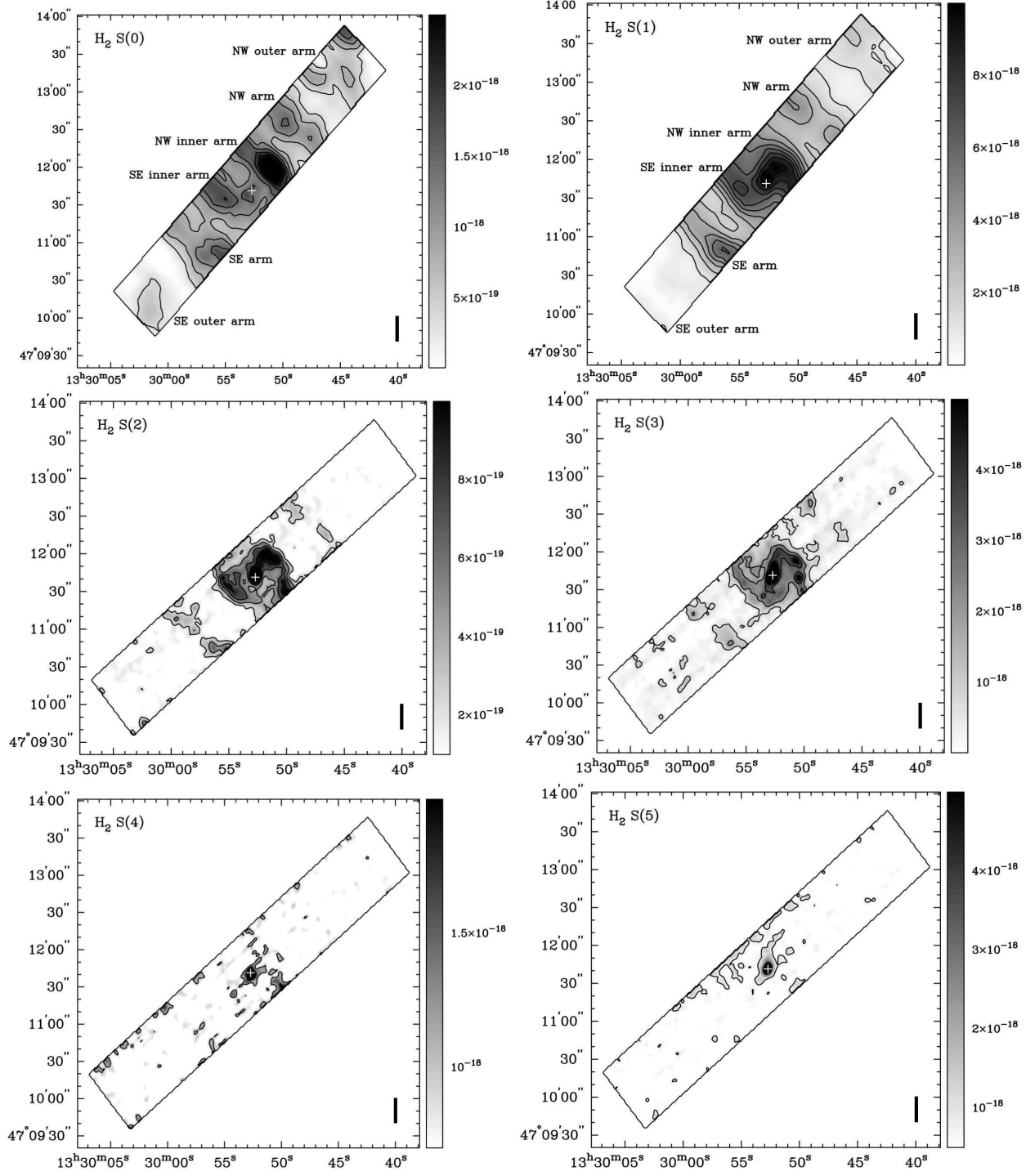
Fig. 1.— Maps of the H_2 S(0) (*top left*), H_2 S(1) (*top right*), H_2 S(2) (*middle left*), H_2 S(3) (*middle right*), H_2 S(4) (*bottom left*), and H_2 S(5) (*bottom right*) line fluxes across the SL and LL strips that we mapped with the *Spitzer* IRS. The H_2 S(0) and H_2 S(1) maps are created from the LL data cube. The H_2 S(2), H_2 S(3), H_2 S(4), and H_2 S(5) maps are created from the SL data cube. The grayscale is in units of W m^{-2}. Contour levels are at 3.7×10^{-19}, 7.3×10^{-19}, 1.1×10^{-18}, 1.5×10^{-18}, 1.8×10^{-18}, 2.2×10^{-18}, and 2.9×10^{-18} W m^{-2} for H_2 S(0); 1.1×10^{-18}, 2.1×10^{-18}, 3.2×10^{-18}, 4.3×10^{-18}, 5.4×10^{-18}, 6.4×10^{-18}, 7.5×10^{-18}, 8.6×10^{-18}, and 9.6×10^{-18} W m^{-2} for H_2 S(1); 2.2×10^{-19}, 4.4×10^{-19}, 6.7×10^{-19}, 8.9×10^{-19}, and 1.1×10^{-18} W m^{-2} for H_2 S(2); 1.3×10^{-18}, 4.0×10^{-18}, 6.7×10^{-18}, 9.4×10^{-18}, and 1.2×10^{-17} W m^{-2} for H_2 S(3); 1.0×10^{-18} and 2.0×10^{-18} W m^{-2} for H_2 S(4); 8.0×10^{-19}, 4.0×10^{-18}, and 7.3×10^{-18}W m^{-2} for H_2 S(5). The vertical axis is the right ascension and the horizontal axis is the declination. In all of the maps, north is up, east is to the left, and the cross denotes the nucleus of the galaxy. The different spiral arm regions are labeled on the H_2 S(0) and H_2 S(1) maps in order to aid in discussing the molecular gas morphologies. The bar in the bottom right corner of the maps represents 1 kiloparsec. The box around the intensity maps represents the SL or LL strip that we mapped.
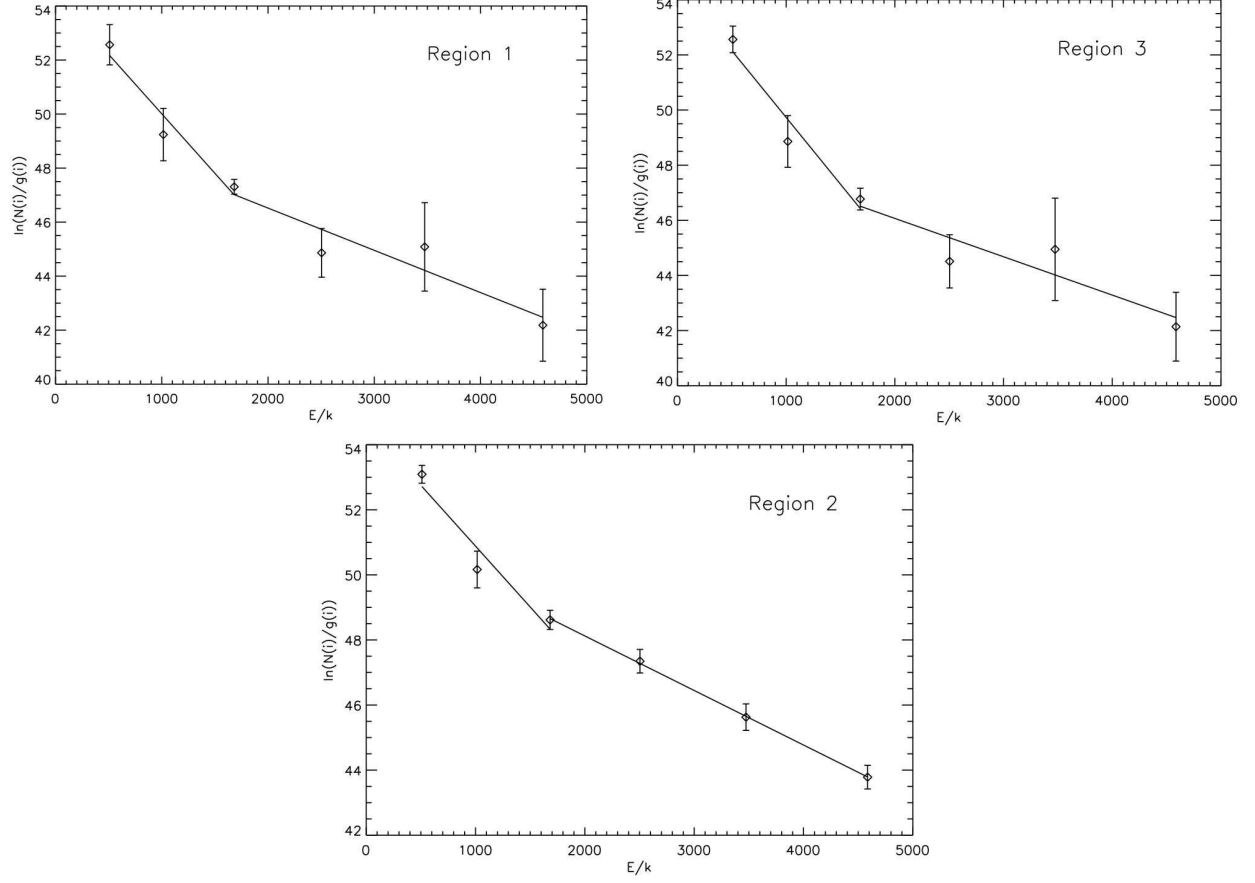
Fig. 2.— Shown are excitation diagrams and the fits to the warm and hot H_2 phases taken from three different single pixel regions along the M51 strip. The different regions are marked on the H_2 surface density maps in Figure 3.
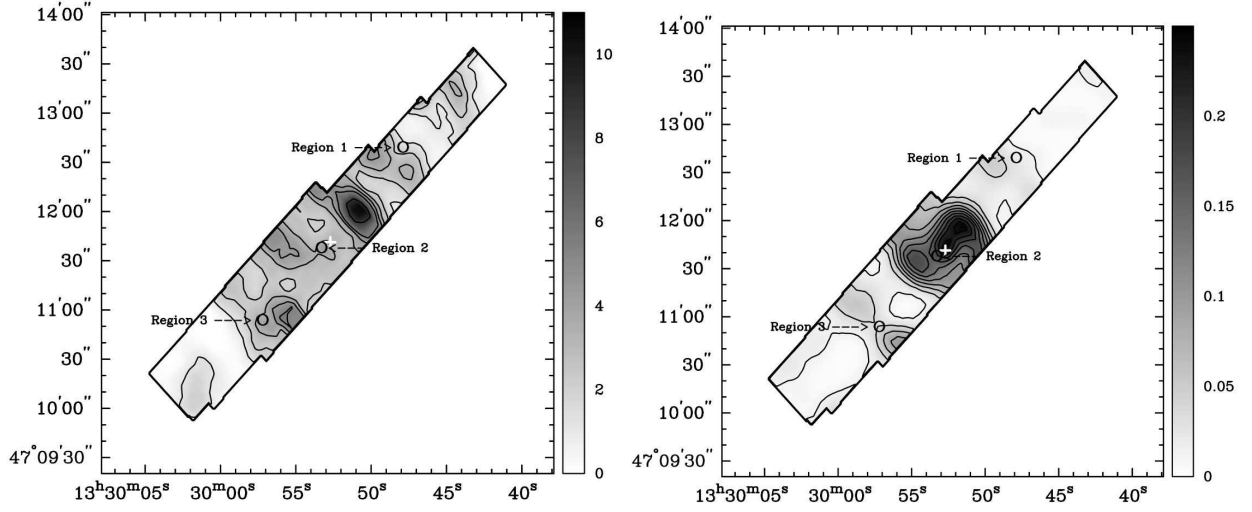
Fig. 3.— Shown are the warm (T = 100 − 300 K) H$_2$ (*left*) and hot (T = 400 − 1000 K) H$_2$ (*right*) surface density distributions. The surface density distributions are in units of M$_\odot$ pc^{-2}. Contours are overplotted for clarity. The warm H$_2$ surface density contour levels are at 1.10, 2.21, 3.32, 4.43, 5.55, and 8.85 M$_\odot$ pc^{-2}. The hot H$_2$ contour levels are at intervals of 10 % of 0.25 M$_\odot$ pc^{-2}. The hot H$_2$ surface density distribution is derived from the fit to the H$_2$ S(2) − H$_2$ S(5) lines and the warm H$_2$ surface density distribution is derived from the fit to the H$_2$ S(0) − H$_2$ S(2) lines, corrected for the contribution of the hot H$_2$ phase. The three circles denote the regions of the excitation diagrams in Figure 2.
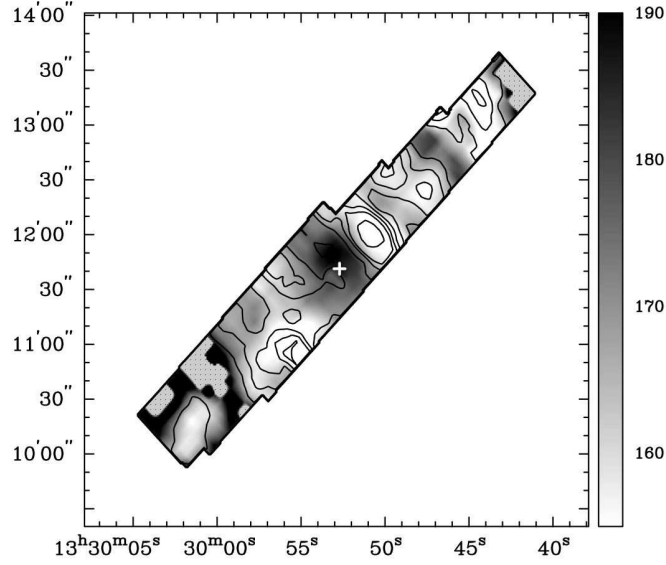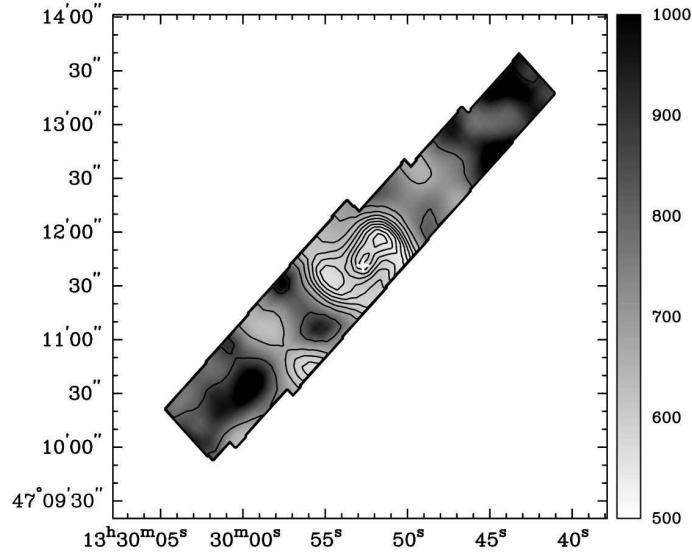
Fig. 4.— The warm (T = 100 − 300 K) H$_2$ surface density distribution (in contours) compared to the warm H$_2$ temperature distribution (in grayscale, in units Kelvin). The warm H$_2$ temperature and surface density distributions are derived from the fit to the excitation diagrams across the strip for the H$_2$ S(0) − H$_2$ S(2) lines, corrected for the contribution of the hot (T = 400 − 1000 K) H$_2$ phase. Surface density contour levels are at 1.10, 2.21, 3.32, 4.43, 5.55, and 8.85 M$_\odot$ pc^{-2} (same as in Figure 3). The non-rectangular shape to the map is due to the slight offset of the *Spitzer* IRS SL strip relative to the LL strip.

Fig. 5.— The hot (T = 400 − 1000 K) H$_2$ surface density distribution (in contours) compared to the hot H$_2$ temperature distribution (in grayscale, in units Kelvin). The hot H$_2$ temperature and surface density distributions are derived from the fit to the excitation diagrams across the strip for the H$_2$ S(2) − H$_2$ S(5) lines. Surface density contour levels are at intervals of 10% of 0.25 M$_\odot$ pc^{-2} (same as in Figure 3).
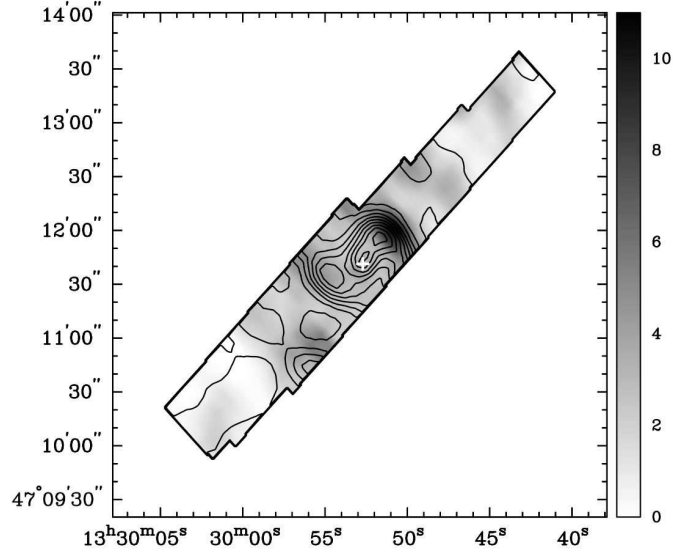
Fig. 6.— The warm (T = 100 − 300 K) H_2 surface density (in grayscale) compared to the hot (T = 400 − 1000 K) H_2 surface density (in contours). Contours levels for the hot H_2 surface density distribution are at intervals of 10% of the maximum surface density (0.25 $M_\odot$ pc^{-2}). The grayscale is in units of $M_\odot$ pc^{-2}.

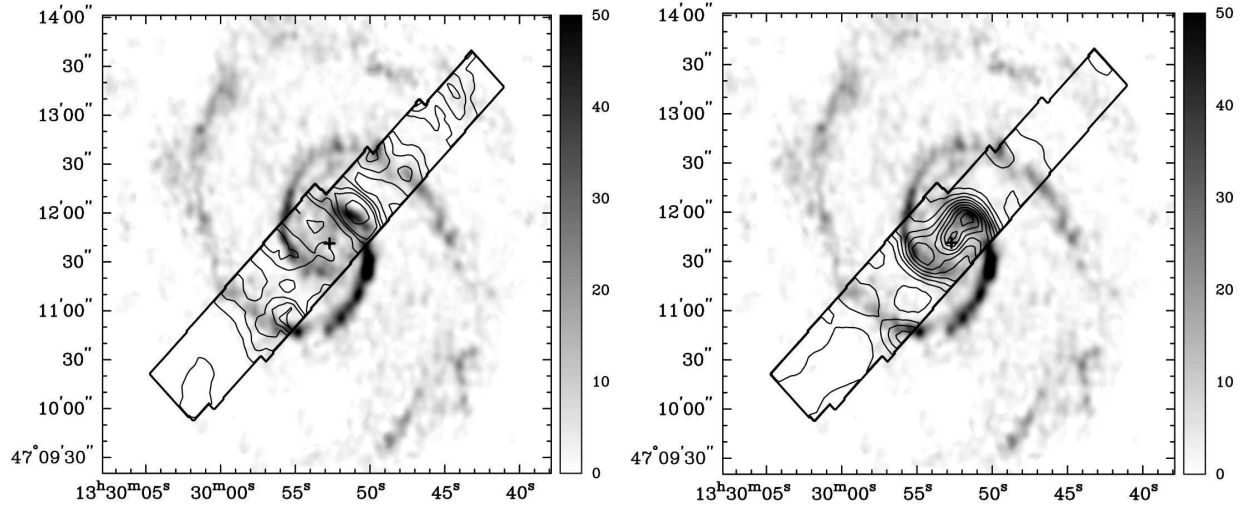Fig. 7.— *Left*: Comparison of CO intensity (in grayscale) to the warm (T = 100 − 300 K) H$_2$ surface density (in contours). The CO intensity is in units of Jy km s^{-1}. The warm H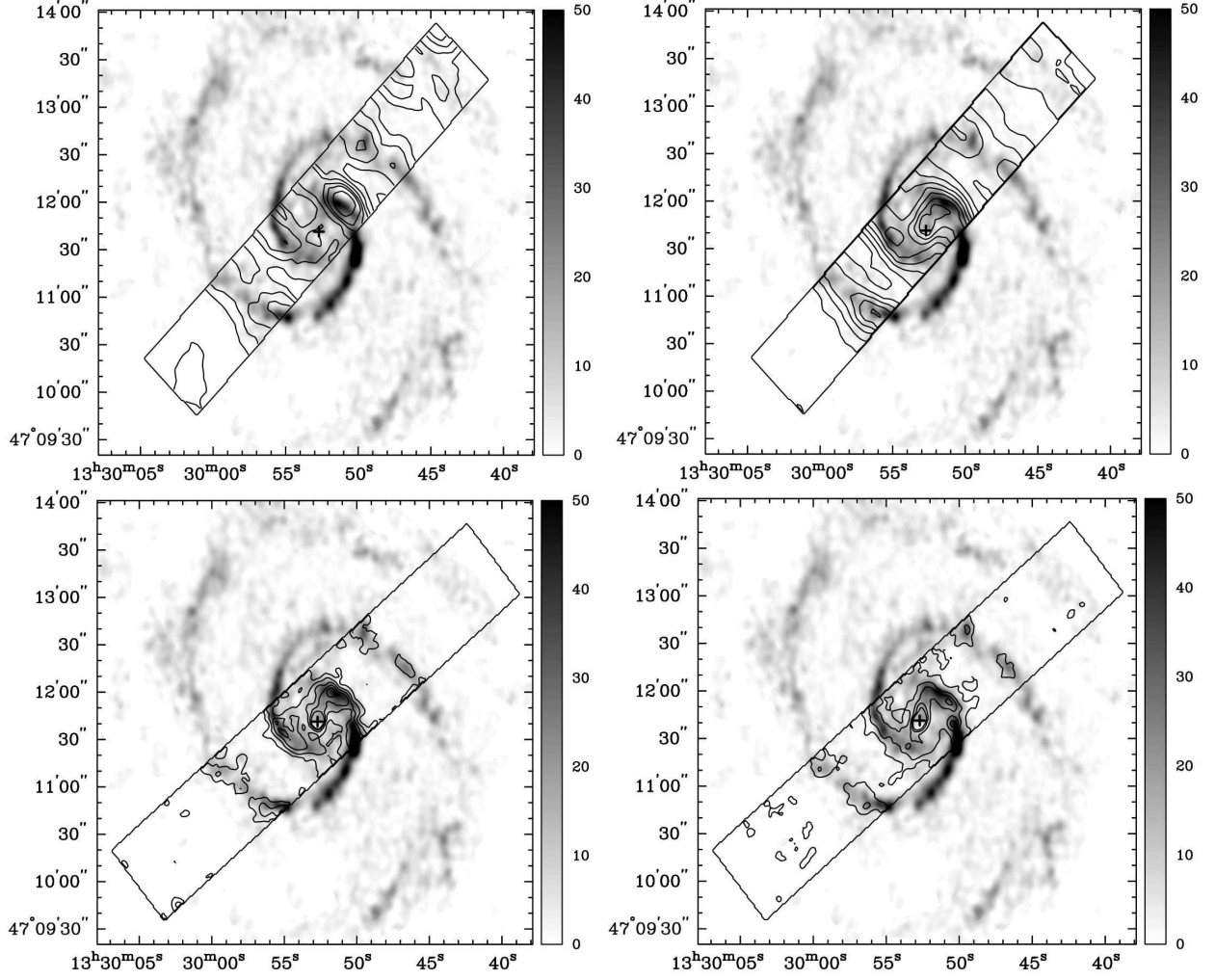$_2$ surface density contours are the same as in Figures 3 and 4. *Right*: Comparison of CO intensity (in grayscale) to the hot (T = 400 − 1000 K) H$_2$ surface density (in contours). The CO intensity is in units of Jy km s^{-1}. The hot H$_2$ surface density contours are the same as in Figures 3 and 5.

Fig. 8.— Comparison of the CO emission to the H$_2$ S(0) (*top left*), H$_2$ S(1) (*top right*), H$_2$ S(2) (*bottom left*), and H$_2$ S(3) (*bottom right*) emission. The CO emission maps are in units of Jy km s^{-1}. Contour levels for H$_2$ S(0), H$_2$ S(1), H$_2$ S(2), and H$_2$ S(3) are the same as in Figure 1.
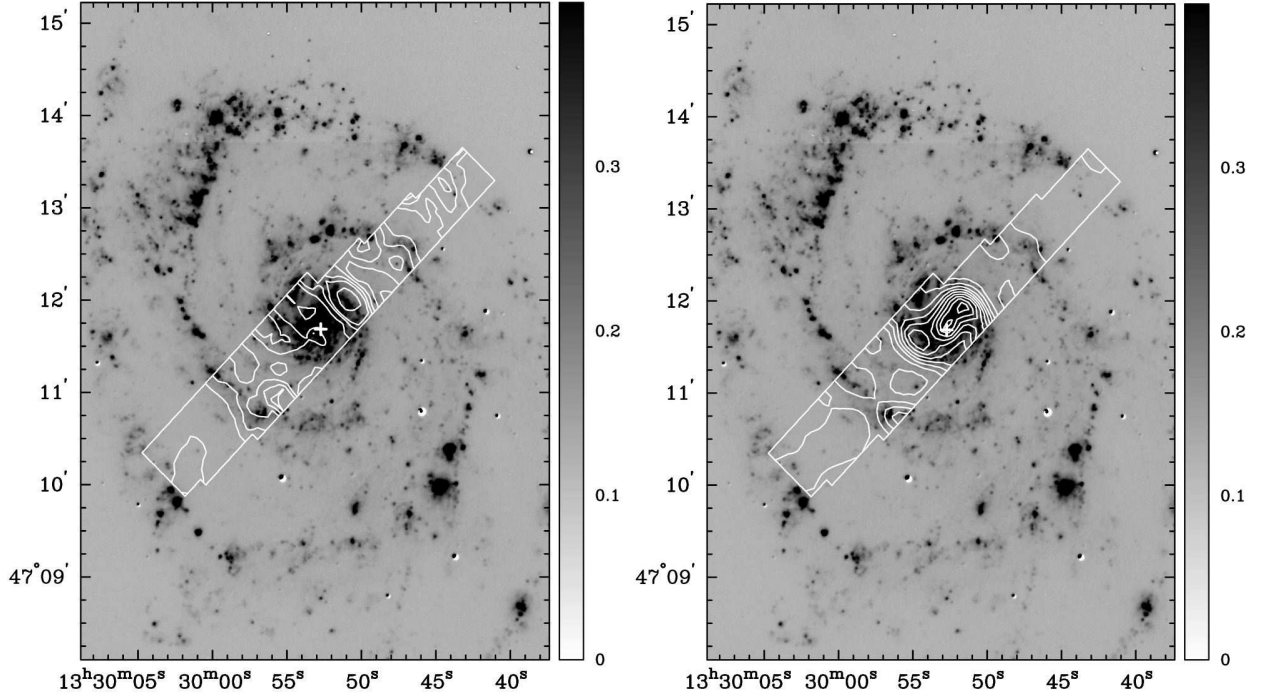
Fig. 9.— *Left*: Comparison of Hα (in grayscale) to the warm (T = 100 − 300 K) H$_2$ surface density (in contours). The Hα image is in units of counts s^{-1}. The warm H$_2$ surface density contours are the same as in Figures 3 and 4. *Right*: Comparison of Hα (in grayscale) to the hot (T = 400 − 1000 K) H$_2$ surface density (in contours). The Hα image is in units of counts s^{-1}. The hot H$_2$ surface density contours are the same as in Figures 3 and 5.
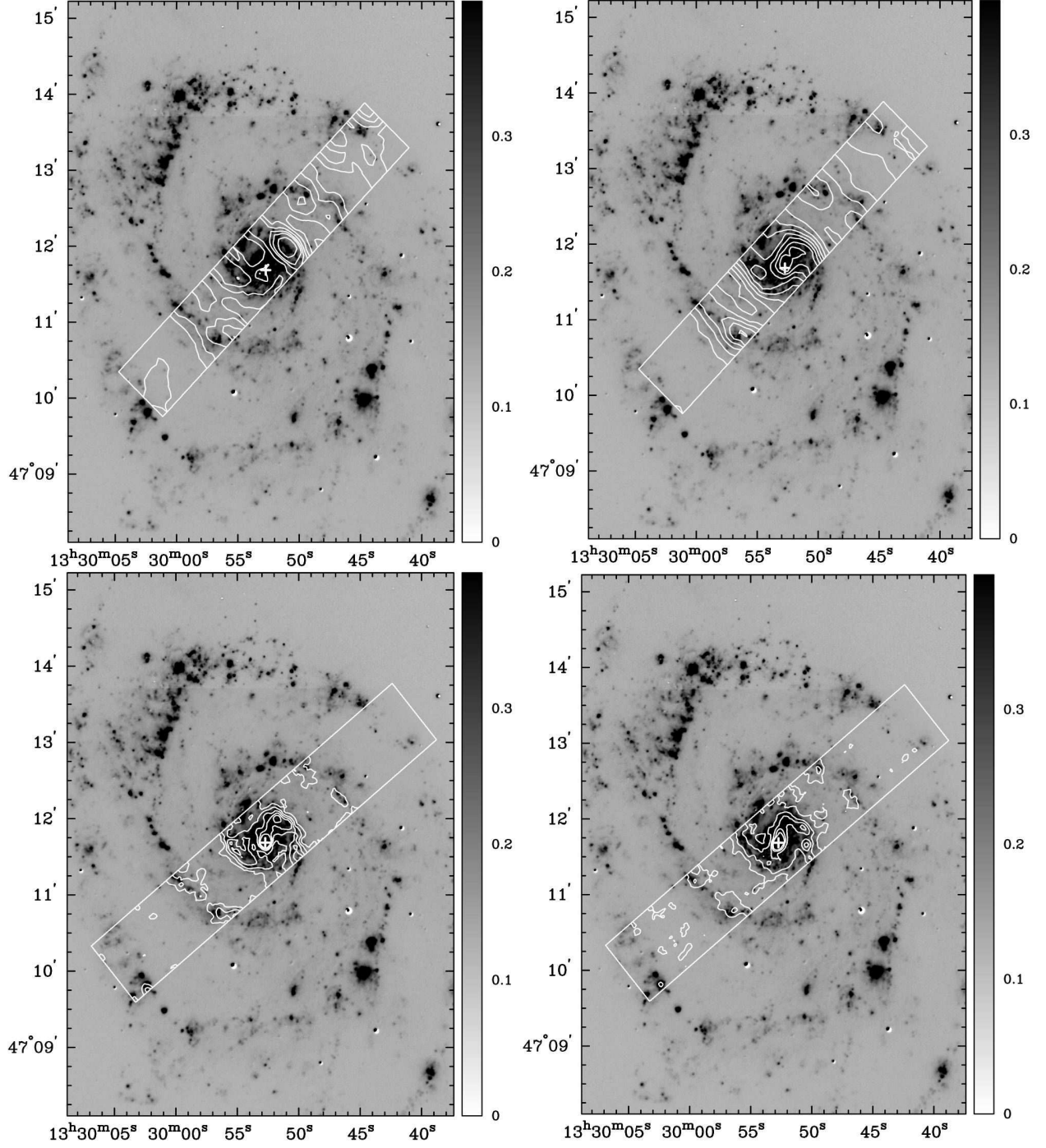
Fig. 10.— Comparison of Hα emission to the H$_2$ S(0) (*top left*), H$_2$ S(1) (*top right*), H$_2$ S(2) (*bottom left*), and H$_2$ S(3) (*bottom right*) emission. The Hα image is in units of counts s^{-1}. Contour levels for H$_2$ S(0), H$_2$ S(1), H$_2$ S(2), and H$_2$ S(3) are the same as in Figure 1.
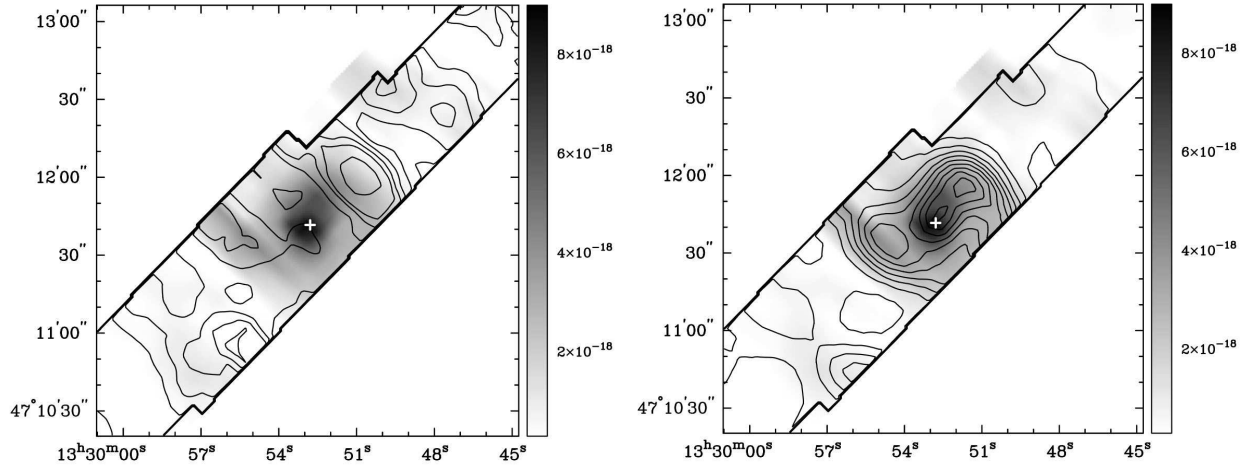
Fig. 11.— *Left*: Comparison of the [O IV](25.89 μm) emission (in grayscale) to the warm (T = 100 K - 300 K) H_2 surface density distribution (in contours). Hot H_2 surface density contours are the same as in Figures 3 and 4. *Right*: Comparison of the [O IV](25.89 μm) emission (in grayscale) to the hot (T = 400 - 1000 K) H_2 surface density distribution (in contours). Hot H_2 surface density contours are the same as in Figures 3 and 5. The [O IV](25.89 μm) emission is in units of W m^{-2}.
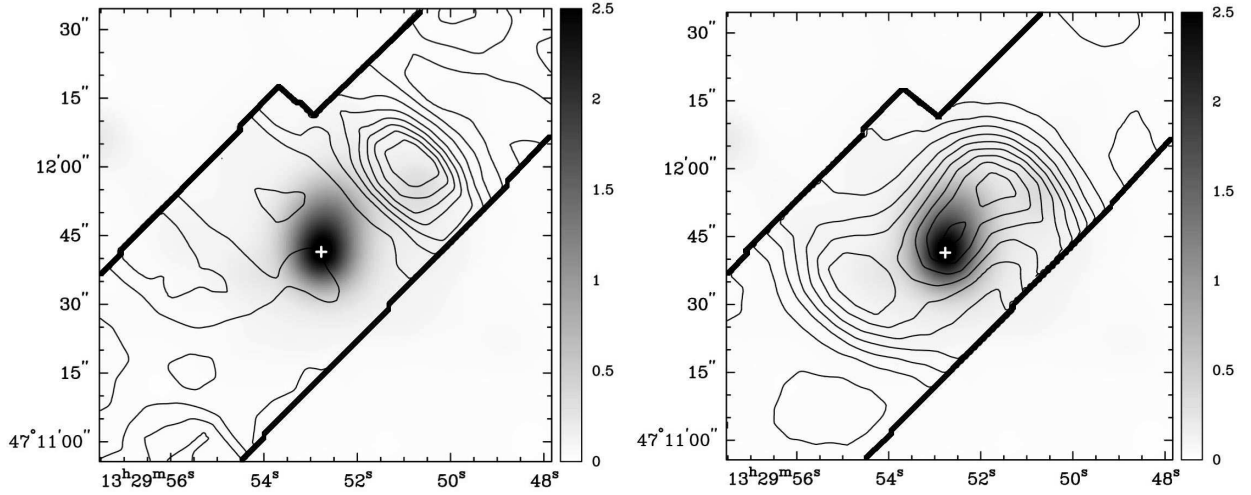
Fig. 12.— *Left*: Comparison of the smoothed $0.5 - 10$ keV X-ray emission band (in grayscale) to the warm (T $= 100 - 300$ K) H_2 surface density distribution (in contours). The X-ray image has been smoothed to the same resolution as the warm H_2 surface density map. X-ray emission is in units of counts. H_2 surface density contours are the same as in Figures 3 and 4. *Right*: Comparison of the smoothed $0.5 - 10$ keV X-ray emission band (in grayscale) to the hot (T $= 400 - 1000$ K) H_2 surface density distribution (in contours). The H_2 surface density distribution contours are the same as in Figures 3 and 5.
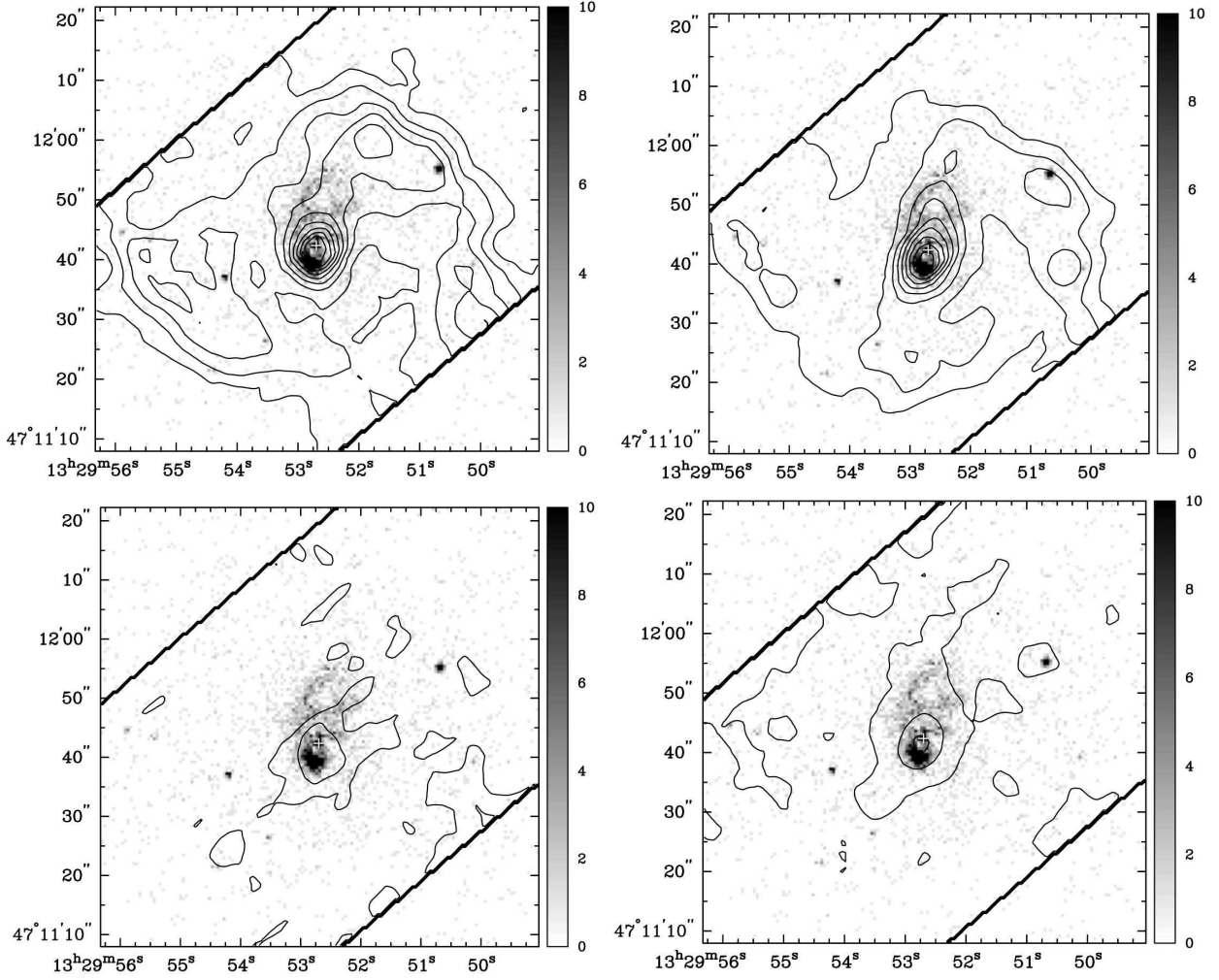
Fig. 13.— Comparison of the $0.5 - 10$ keV X-ray emission band (in grayscale) to the H_2 S(2) (*top left*), H_2 S(3) (*top right*), H_2 S(4) (*bottom left*), and H_2 S(5) (*bottom right*) emission in the nuclear region of M51. X-ray emission is in units of counts. The H_2 S(2) and H_2 S(3) emission contours are at 10 % of their peak values (2.20×10^{-18} and 1.35×10^{-17} W m^{-2}, respectively). The H_2 S(4) contours are at 1.0×10^{-18} and 2.0×10^{-18} W m^{-2} and the H_2 S(5) contours are at 8.0×10^{-19}, 4.0×10^{-18}, and 7.3×10^{-18} W m^{-2}.

Table 1.   H$_2$ Parameters

Transition	Wavelength (μm)	Rotational State (J)	Energy (E/k)	A (s^{-1})	Statistical Weight (g)
H$_2$(0-0)S(0)	28.22	2	510	2.94×10^{-11}	5
H$_2$(0-0)S(1)	17.04	3	1015	4.76×10^{-10}	21
H$_2$(0-0)S(2)	12.28	4	1682	2.76×10^{-9}	9
H$_2$(0-0)S(3)	9.66	5	2504	9.84×10^{-9}	33
H$_2$(0-0)S(4)	8.03	6	3474	2.64×10^{-8}	13
H$_2$(0-0)S(5)	6.91	7	4586	5.88×10^{-8}	45

Note. — The statistical weight (g) is $(2J+1)(2I+1)$ where I equals 1 for odd J transitions (ortho transitions) and I equals 0 for even J transitions (para transitions).